Restrictions on the Field of View for an Undersampled 1-D Synthetic Thinned Aperture Radiometry

Boon H Lim[1], Ruba Amarin[2], Salem El-Nimri[2], James Johnson[2], Linwood Jones[2] and Christopher S Ruf[1]

1. University of Michigan
Ann Arbor, MI USA 48109-2143
bhlim@umich.edu

2. University of Central Florida
Orlando, FL USA 32816-2362
ramarin@mail.ucf.edu

Abstract – Traditional radio astronomy formulation of the field of view (FOV) applied to a non-Nyquist spatially sampled synthetic thinned aperture radiometers appear to overestimate the FOV. Utilizing the current design of the Hurricane Imaging Radiometer (HIRad) as a baseline instrument, a simple analytical instrument simulator is developed to investigate the different methods of determining the FOV. Analytically, this value is found to be 70^0. However the usable range seems to extend only to 61^0. The presence of aliased grating lobes is easily seen in the synthesized antenna patterns. Beam efficiency plots with threshold levels can be used to determine the reduced FOV. Error analysis is performed utilizing several sample images of Hurricane Katrina.

I. INTRODUCTION

Synthetic thinned aperture radiometers (STAR) have several benefits as compared to their real aperture counterparts. For an instrument such as the proposed Hurricane Imaging Radiometer (HIRad), a 1-D STAR operated in a push-broom mode, a wide field of view is achieved simultaneously and continuously without the need of a scanning antenna [**1**]. By comparison, the current operational Stepped Frequency Microwave Radiometer (SFMR) only has a single nadir pointing pixel. The current preliminary HIRad design will be used as the baseline instrument for this analysis.

Key parameters that determine the characteristics of a STAR are the antenna linear array unit spacing (d_λ) and the maximum unit spacing (D). These two parameters determine the usable field of view (FOV) and pixel resolution, respectively. Notably, values of the unit spacing larger than d_λ =0.5 have a reduced field of view since they are not spatially sampled at the Nyquist rate [2]. For HIRad, utilizing the current design parameters, only the 7 GHz channel does not satisfy this condition. In this work, the extent of the usable field of view is determined through a variety of methods, including the traditional radio astronomy formulation. The traditional formulation of FOV is calculated by determining the first null of the system array factor [**2**]. Using (1), the off nadir FOV extent for the 7 GHz HIRad channel is found to be approximately 70^0.

$$\theta_{UFOV} = \sin^{-1}\left(\frac{1}{2d_\lambda}\right) \quad (1)$$

A HIRad instrument simulator has been developed that calculates visibilities for a given brightness temperature distribution under observation. The simple 1-D forward model gives reasonable results since the real aperture of the elemental antenna array gives an appropriate thin fan beam. The reconstruction algorithm will include the effects of an antenna pattern and aperture tapering may be applied to determine their effect on the synthesized antenna pattern and eventually image retrieval.

The extent of the FOV is estimated from the synthesized antenna patterns by locating the appearance of aliased grating lobes. Another crude estimate can be found by reconstructing a scene with significant contrast such as a step function. Plots of the beam efficiency at each pixel clearly show the appearance of the grating lobes as the curve dips significantly. An appropriate threshold is recommended for determination of the FOV.

SFMR measurements of Hurricane Katrina will be used to determine the effectiveness of the restricted field of view and the effect of tapering the aperture. The scenes to be investigated include flights over the eye, eye wall and a position with maximum grating lobe contamination.

II. HIRAD INSTRUMENT DESCRIPTION

The HIRad instrument will be used as the basis for this analysis. The current operational instrument for hurricane ocean surface wind speed and rain rate measurement has been the SFMR which provides a single nadir looking pixel and scans from 5 to 8 GHz over 8 channels [**1**]. HIRad will be configured as a 10 element synthetic thinned radiometer array to provide wide swath coverage with high pixel resolution.

Each element will consist of 32 multi-resonant dipoles in a linear broadside array configuration, oriented along track so that the fan beam defines the cross track field of view [**3**]. The physical spacing between the resonant antennas in the real aperture will be 1.5 inches. The optimal configuration for a 10 element array is a maximum unit spacing, D, of 36 [**4**]. The unit spacing between the antenna array elements is currently set at 0.9 inches. HIRad will operate at 4 resonant frequencies – 4, 5, 6 and 7 GHz – and the unit spacing, d_λ, between the antenna elements (defined as the physical distance divided by the wavelength) varies according on the frequency of observation.

III. Visibility Forward Model Definitions

A. Complex Visibilities

The complex visibilities measured by the radiometer are a function of the scene observed, $T_B(\theta,\phi)$, the element antenna patterns and the interference patterns between the particular antennas [**5**]. This is defined by (2)

$$V(u,v)=\int_0^{2\pi}\int_0^{\pi} T_B(\theta,\phi)F(\theta,\phi)e^{j2\pi(u\sin\theta\cos\phi+v\sin\theta\sin\phi)}\sin\theta d\theta d\phi \quad (2)$$

$$where\ u=D_x/\lambda\ \ and\ \ v=D_y/\lambda$$

For a 1-D imager such as HIRad, (2) reduces to (3). The limits of θ are modified to reflect that only the half-space below the imager is considered.

$$V(u)=\int_0^{2\pi}\int_0^{\pi/2} T_B(\theta,\phi)F(\theta,\phi)e^{j2\pi(u\sin\theta\cos\phi)}\sin\theta d\theta d\phi \quad (3)$$

The number of available visibilities is a function of the maximum unit spacing for a properly sampled thinned array. Due to the Hermitian symmetry of the visibility function, $\left(V(u,v)=V^*(-u,-v)\right)$, this number is double that of the maximum unit spacing (D). Therefore the total number of visibilities available N is equal to 2D+1, where the 'plus 1' addition accounts for the 'zeroth visibility' or the total power measurement of the scene [**6**].

B. Assumptions

Several assumptions are made in this formulation. The fringe wash function, which defines the decorrelation of the target signal away from nadir, is neglected and assumed to be negligible. Antenna element patterns are also assumed to be identical for each of the correlated antenna pairs. For the simulations, a simple dipole antenna pattern is used while the actual antenna elements are still being developed. Often, visibilities will be calculated based purely on a 1 dimensional (1-D) forward model as shown in (4). This simplified forward model will be used to create all model visibilities to be used in image reconstruction.

$$V(u)=\int_{-\pi/2}^{\pi/2} T_B(\theta)F(\theta)e^{j2\pi(u\sin\theta)}\sin\theta d\theta \quad (4)$$

C. Matrix Representation

The relationship between the visibilities and the observed scene is most easily represented in matrix form [**7**]. Given N, the number of visibilities and P, the pixel resolution of the scene, we arrive at (5) where G is the pseudo 'gain matrix' (G-Matrix) of the system [**6**].

$$\underset{(Nx1)}{V} = \underset{(NxP)}{G}\underset{(Px1)}{T_B} \quad (5)$$

The G-Matrix contains the elements of interest, the antenna pattern and sampling affects if derived from (4). The G-Matrix can be found analytically by assuming ideal antenna patterns or experimentally from anechoic chamber measurements [**6**].

IV. Image Reconstruction Algorithm

A. 1-D Reconstruction with Antenna Pattern

From (5), if the inverse of the G-Matrix can be found, the relationship between the estimated brightness temperatures $\hat{T}_B$ and the visibilities can be represented by (6).

$$\underset{(Px1)}{\hat{T}_B} = \underset{(PxN)}{G'}\underset{(Nx1)}{V} \quad (6)$$

$$where\ G'=G^t(GG^t)^{-1}$$

G' is the termed the reciprocal basis to G and is determined using the Moore-Penrose matrix inverse, which minimizes the difference between the true image and the reconstructed image [**6**]. This will be apparent during the discussion of the synthesized antenna pattern.

B. The Synthesized Antenna Pattern

Making the substitution of (6) into (5) directly yields the relationship between $\hat{T}_B$ and T_B (7). The matrix $G'G$ is known as the synthesized antenna pattern [**7**]. Each row of this matrix represents the contribution of each pixel in the measured scene to the corresponding pixel in the estimated scene.

$$\underset{(Px1)}{\hat{T}_B} = \underset{(PxP)}{[G'G]}\underset{(Px1)}{T_B} \quad (7)$$

It is important to note that the synthesized antenna patterns can have negative side lobes if incoming signals in the interferometric system are out of phase. Note that in (7) the represented matrix $G'G$ is shown to be square. This condition is not necessary as $\hat{T}_B$ may be sampled differently and retrieved to a different extent from the input scene.

V. Simulator Performance Metrics

Evaluation of the simulator and the synthesized antenna patterns, borrows heavily from standard antenna terminology with minor modifications. While metrics such as first side lobe level, 3 dB beamwidth and null beamwidth can be used directly, others such at the beam efficiency must be modified slightly. Included in the discussion are beam efficiency curves that perform well in detecting the presence of grating lobes.

Crude estimates of the FOV can also be obtained from the full synthesized antenna pattern for every pixel.

A. Aliased Grating Lobe Appearance

Fig. 1 shows the full synthetic aperture pattern for all pixels for the 7 GHz HIRad channel. The circled areas show the appearance of the grating lobes at the higher incidence angles.

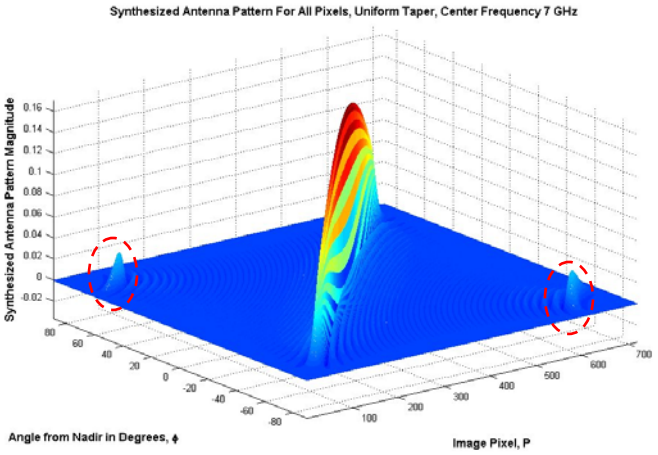

Figure 1: Full synthesized antenna pattern. Grating lobes begin to appear at the large incident angles.

Fig. 2 shows the synthetic aperture pattern for two pixels, nadir pointing and at -70^0, that have been normalized and plotted in dB. The nadir pointing pixel shows clearly the -6.7 dB side lobe level for a uniform taper. For the -70^0 pixel, the magnitude of contamination from the grating lobe is equal to that in the main beam. From this plot it is apparent that FOV should be restricted.

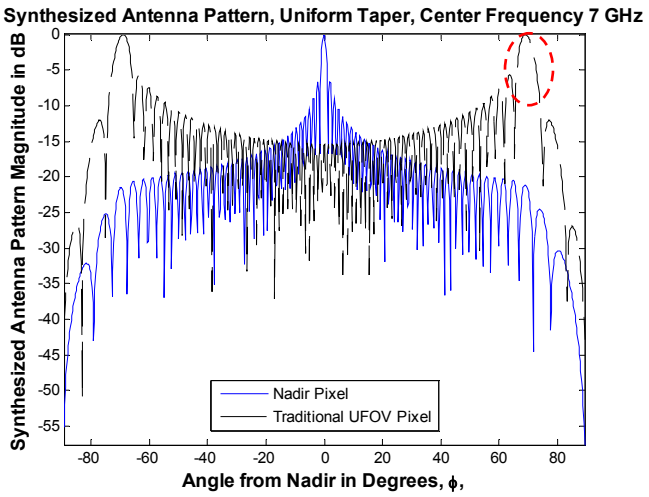

Figure 2: Synthesized antenna pattern for pixels at nadir and -70^0. Grating lobe of equal magnitude to the main beam appears at $+70^0$

B. Beam Efficiency, η_p

Traditional beam efficiency calculations yield results greater than 1 due to the presence of the negative sidelobes. (8) shows the beam efficiency, η_p, at pixel p calculated for a null to null extent (3dB beamwidth calculation is also possible). Alternative forms have been proposed, such as using the absolute or the squared values [**6**] such that magnitudes do not exceed unity.

$$\eta_p = \frac{\int_{\theta_{l\_null}}^{\theta_{u\_null}} AF_p(\theta)d\theta}{\int_{-\pi/2}^{\pi/2} AF_p(\theta)d\theta} \tag{8}$$

where $AF_p(\theta)$ *is the corresponding p'th row of* $G'G$

θ_{u_null} *and* θ_{l_null} *define the main beam null extent*

Fig. 3 shows two different curves, one with the traditional formulation and one with the squared definition. Both exhibit significant loss in the beam efficiency as the grating lobes appear. Recall, for this idealized system, the synthesized antenna patterns are symmetric around nadir. At 70^0 from nadir the level drops by the predicted level of 50% for both definitions. Markers have been placed at 98% of the maximum value. The reduced FOV for this particular stringent threshold is approximately 61^0 utilizing the traditional definition.

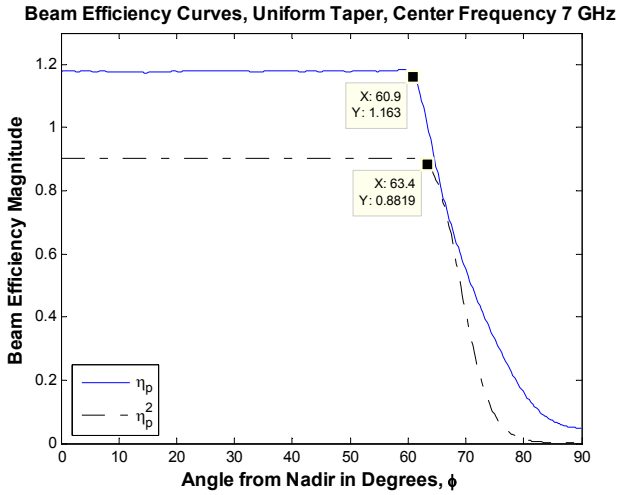

Figure 3: Beam efficiency curves out to the full field of view and a threshold level of 98% of the maximum.

VI. Hurricane Katrina Sample Data

Sample SFMR data is available from over flights of Hurricane Katrina on August 28th 2005. Apparent brightness temperatures are computed from these flights and converted by Central Florida Remote Sensing Laboratory (CFRSL) into sample swaths that would be measured by a HIRad type instrument flying at 11 km and the appropriate incident angles. Three such swaths are provided, the first with the nadir looking pixel positioned over eastern eye wall of the hurricane, the second with the nadir looking pixel positioned such that the an eyewall is just outside a grating lobe, and the third with the nadir looking pixel positioned such that the eye wall was in the area of an aliased grating lobe.

Fig. 4 shows the reconstruction of the first scene (over eye-wall) for the full field of view out to 90^0. Errors increase

dramatically at the larger incidence angles. Taking the difference between the retrieved scene and the input scene, we arrive at an estimate to the error in the system. The pixel resolution of the input scene is significantly higher than that which can be resolved by the HIRad instrument. The high frequency components in the input scene will not be imaged in the retrieved scene.

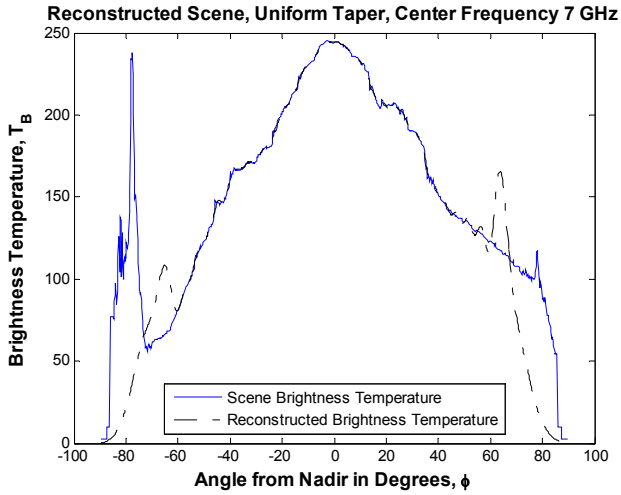

Figure 4: Reconstructed scene from input swath with nadir over the eye wall.

Fig. 5 shows the difference in the retrieved scene and input scene up to the traditional FOV of 70^0. The dashed lines represent the recommended restricted FOV extent as determined by a 98% threshold defined previously. It is apparent that the aliased grating lobes introduce significant errors to the measurements past this level. Within the restricted FOV, the errors in the measurement are often less than 1%.

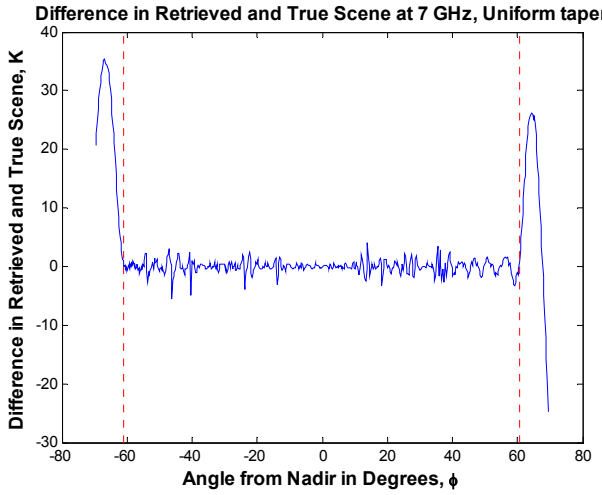

Figure 5: Difference in the retrieved and true scene. Dashed lines indicate the recommended restricted FOV.

All three swaths show similar behavior in the difference between the input and retrieved scenes. Note that not all the error in the reconstructed scene can be attributed to the STAR imager. A better comparison should be made with a real aperture imager that has the same beamwidth as the STAR imager. This work is currently in progress, as well as the comparison of the performance of various tapers.

VII. Conclusions

The FOV of a 1-D STAR cannot be simply defined by the traditional formulation of the null extent of the array factor. At this extent, the contribution of the aliased grating lobe is equal to that of the main beam in questions. A simple 1-D instrument simulator is developed for the proposed HIRad instrument. From the synthesized antenna patterns at 7 GHz, grating lobes can easily be seen since d_λ is greater than 0.5 wavelengths.

Beam efficiencies are calculated for every pixel in the synthesized antenna pattern. It is evident from Fig. 3 where the grating lobes appear and begin to reduce the efficiency adversely. A threshold of 98% of the maximum is recommended to determine the restricted FOV. For the HIRad 7 GHz channel, the extent of the FOV is reduced from 70^0 to approximately 61^0.

Sample images retrieved from SFMR data show that the errors within the restricted FOV are significantly smaller compared to those with aliased signals. Additional work with aperture tapers needs to be performed to determine the most effective taper for the various sample scenes.

VIII. References

[1] Jones, W.L., J.-D. Park, J. Zec, C.S. Ruf, M.C. Bailey and J.W. Johnson, "A Feasibility Study for a Wide-Swath, Airborne, Hurricane Imaging Microwave Radiometer for Operational Hurricane Measurements," Proc. of the 2002 IEEE International Geoscience and Remote Sensing Symposium, Toronto, CA, 24-28 June 2002.

[2] J. D. Kraus, Radio Astronomy, McGraw Hill, 1966

[3] C. S. Ruf, "HIRad Instrument Design Technical Report," 20 Dec. 2004.

[4] C. S. Ruf "Numerical Annealing of Low-Redundacy Linear Arrays," *IEEE Trans. Ant. And Prop*, vol. 41, pp. 85–90, Jan.1993.

[5] C. S. Ruf, C. T. Swift, A. B. Tanner, and D. M. Le Vine, "Interferometric synthetic aperture microwave radiometry for the remote sensing of the earth," *IEEE Trans. Geosci. Remote Sensing*, vol. 26, pp. 597–611, Sept.1988.

[6] A. B. Tanner and C. T. Swift, "Calibration of a synthetic aperture radiometer," *IEEE Trans. Geosci. Remote Sensing*, vol. 31, pp. 257–267, Jan. 1993.

[7] M. A. Goodberlet, "Improved Image Reconstruction Techniques for Synthetic Aperture Radiometers," *IEEE Trans. Geosci. Remote Sensing*, vol. 38, pp. 1362–1366, May 2000.